

**DEVELOPMENT OF RICE STARCH
MICRONEEDLES FOR DRUG DELIVERY TO
THE SKIN**

BILAL HARIETH MAHMOOD ALRIMAWI

UNIVERSITI SAINS MALAYSIA

2023

**DEVELOPMENT OF RICE STARCH
MICRONEEDLES FOR DRUG DELIVERY TO
THE SKIN**

by

BILAL HARIETH MAHMOOD ALRIMAWI

**Thesis submitted in fulfilment of the requirements
for the degree of
Doctor of Philosophy**

April 2023

ACKNOWLEDGEMENT

First and foremost, praises and thanks to the God almighty for granting me the strength and capability to complete this work.

I would love to express my heartfelt gratitude and appreciation for my main supervisor, Dr. Goh Choon Fu for giving me the opportunity to embark on this journey. Thanks for your valuable guidance and continuous support that helped me through my study and gave me the power to reach this stage. I am truly thankful for your encouragement words and your kindness. You have been a great mentor, advising on a research topic, being available and responding to my questions. Studying under your supervision will always be one of my best memories in Malaysia.

I would also like to show my full gratitude and appreciation to my co-supervisor, Dr Ng Keng Wooi for his support, guidance, and encouragement. Your kind words made me stronger and gave me the confidence to finish my work.

I would like to express special thanks to Associate Professor Dr Chan Siok Yee for her support and encouragement during my work.

I would like to share my love and gratitude to my parents who deserve all the credit for my achievements. They have supported and encouraged me to continue my postgraduate studies. They have shown me all the love and trust that I needed. Without them, I would never be the person who I am today. Great thanks and love to my brother and sisters for their magnificent love, support, and encouragement.

I am using this opportunity to share my gratitude and love to my precious friends who became brothers during this journey, Dr Al-Mashhadani Abdul Salam Qahtan, Dr Dayoob Mohammad, Dr Alshara Ahmad Yassin, Mohammad Al-Thiabat, Ghazi Al-Jabal, Obada Sawafta, Ahmad Alassas, Amer Abdul Hafez, Zahra Suleiman, Fadi Ghassan and Nadeem Al Ameen. I am thankful for all the great moments and memories that we have been through. Special thanks and gratitude to my friends and lab mates of the Skin Research Group, Wong Li Ching, Estee Lee, Dr. Shakho Shahad, Yee Shan Sim, Yeoh Soo Chin, Yimo Liang, and Hailong Yu for their great support and help. I enjoyed every moment during my lab work, and that would not be happened without them.

TABLE OF CONTENTS

ACKNOWLEDGEMENT	ii
TABLE OF CONTENTS	iv
LIST OF TABLES	xii
LIST OF FIGURES	xiv
LIST OF SYMBOLS	xxi
LIST OF ABBREVIATIONS	xxii
LIST OF APPENDICES	xxiv
ABSTRAK	xxv
ABSTRACT	xxviii
CHAPTER 1 INTRODUCTION	1
1.1 Overview.....	1
1.2 Skin	2
1.2.1 Skin structure	2
1.2.2 Dermal drug delivery	4
1.3 Microneedles (MNs)	6
1.3.1 Definition and history of MNs.....	6
1.3.2 MN types.....	10
1.3.2(a) Solid MNs.....	10
1.3.2(b) Coated MNs	11
1.3.2(c) Hollow MNs	11
1.3.2(d) Hydrogel-forming MNs	12
1.3.2(e) Dissolving MNs	13
1.3.3 Fabrication of dissolving MNs.....	14
1.3.3(a) Polymers used in the fabrication of dissolving MNs	16
1.3.3(a)(i) Polyvinyl pyrrolidone (PVP).....	17

	1.3.3(a)(ii) Polyvinyl alcohol (PVA)	18
	1.3.3(a)(iii) Polysaccharides	20
1.4	Starch	22
	1.4.1 Gelatinisation and retrogradation.....	23
	1.4.2 Rice starch (RSC)	25
	1.4.3 Pharmaceutical applications of RSC.....	27
1.5	Model drugs	31
	1.5.1 Lidocaine hydrochloride (LID).....	31
	1.5.2 Ketoprofen (KTP)	33
1.6	Problem statement.....	36
1.7	Thesis objectives	37
	CHAPTER 2 FORMULATION AND CHARACTERISATION OF RICE STARCH-BASED MICRONEEDLES	38
2.1	Introduction.....	38
2.2	Materials and methods	40
	2.2.1 Materials	40
	2.2.2 Extraction of RSC	41
	2.2.3 Determination of total starch, amylose, and amylopectin content of RSC	42
	2.2.4 Formulation of RSC-based films	43
	2.2.5 Characterisation of RSC-based films.....	44
	2.2.5(a) Attenuated total reflectance fourier transform infrared (ATR-FTIR) spectroscopy	44
	2.2.5(b) Differential scanning calorimetry (DSC).....	45
	2.2.5(c) Mechanical studies.....	46
	2.2.5(d) Dissolution studies.....	48
	2.2.6 Formulation of MN arrays from RSC blends with PVA or PVP	48
	2.2.7 Characterisation of RSC-based MN arrays.....	49

2.2.7(a)	ATR-FTIR spectroscopy.....	49
2.2.7(b)	DSC.....	50
2.2.7(c)	Determination of MN shape and geometry.....	50
	2.2.7(c)(i) Optical microscopy.....	50
	2.2.7(c)(ii) Scanning electron microscopy (SEM)	50
2.2.7(d)	Mechanical studies.....	51
	2.2.7(d)(i) MN %compression test.....	51
	2.2.7(d)(ii) Axial compression test.....	51
2.2.7(e)	MN insertion and penetration.....	52
	2.2.7(e)(i) Parafilm® insertion study.....	52
	2.2.7(e)(ii) <i>In vitro</i> insertion in porcine skin.....	53
2.2.7(f)	MN dissolution studies.....	54
	2.2.7(f)(i) Dissolution of MN in gelatine blocks.....	54
	2.2.7(f)(ii) <i>In vitro</i> MN dissolution in the skin.....	55
2.2.8	Statistical analysis.....	55
2.3	Results and discussion.....	56
2.3.1	Determination of total starch, amylose, and amylopectin content of RSC.....	56
2.3.2	Characterisation of RSC-based films.....	57
	2.3.2(a) Visual observation.....	57
	2.3.2(b) ATR-FTIR spectroscopy.....	59
	2.3.2(c) DSC.....	63
	2.3.2(d) Mechanical studies.....	70
	2.3.2(e) Dissolution of RSC-based films.....	72
2.3.3	Formulation of MN arrays of RSC blends with PVA or PVP.....	74
2.3.4	Characterisation of RSC-based MNs.....	74
	2.3.4(a) MN shape and geometry.....	74

2.3.4(b)	MN %compression test.....	78
2.3.4(c)	Parafilm [®] insertion study	80
2.3.4(d)	Dissolution in gelatine blocks.....	83
2.3.5	Correlation between MNs and films	85
2.3.5(a)	Mechanical properties.....	85
2.3.5(b)	Dissolution	87
2.3.5(c)	ATR-FTIR spectroscopy.....	88
2.3.5(d)	DSC.....	89
2.3.6	Characterisation of PVA20-MN and PVP40-MN	92
2.3.6(a)	SEM	92
2.3.6(b)	ATR-FTIR spectroscopy.....	95
2.3.6(c)	Axial compression test.....	98
2.3.6(d)	<i>In vitro</i> skin insertion and penetration depth	100
2.3.6(e)	<i>In vitro</i> MN dissolution in the skin.....	104
2.4	Conclusions.....	105
CHAPTER 3 LOADING A HYDROPHILIC MODEL DRUG INTO RICE STARCH-BASED MICRONEEDLES		107
3.1	Introduction.....	107
3.2	Materials and methods	108
3.2.1	Materials	108
3.2.2	Formulation of LID-loaded RSC-based MN arrays.....	109
3.2.3	High-performance liquid chromatography (HPLC).....	109
3.2.4	Characterisation of LID-loaded RSC-based MN arrays	110
3.2.4(a)	Determination of MN shape and geometry.....	110
	3.2.4(a)(i) Optical microscopy.....	110
	3.2.4(a)(ii) SEM.....	110
3.2.4(b)	ATR-FTIR spectroscopy.....	110
3.2.4(c)	DSC.....	111

3.2.4(d)	Mechanical studies.....	111
	3.2.4(d)(i) MN %compression test.....	111
	3.2.4(d)(ii) Axial compression test.....	111
3.2.4(e)	MN insertion.....	112
	3.2.4(e)(i) Parafilm [®] insertion study.....	112
	3.2.4(e)(ii) <i>In vitro</i> insertion in porcine skin.....	112
3.2.4(f)	<i>In vitro</i> MN dissolution in the skin.....	112
3.2.4(g)	Drug content and distribution.....	112
3.2.4(h)	<i>In vitro</i> drug release study.....	113
3.2.4(i)	<i>In vitro</i> permeation and mass balance studies.....	115
3.2.5	Statistical analysis.....	116
3.3	Results and discussion.....	117
3.3.1	MN shape and geometry.....	117
3.3.2	Mechanical studies.....	118
3.3.3	Parafilm [®] insertion study.....	120
3.3.4	<i>In vitro</i> skin insertion.....	122
3.3.5	SEM.....	124
3.3.6	ATR-FTIR spectroscopy.....	125
3.3.7	DSC.....	130
3.3.8	Axial compression test.....	135
3.3.9	<i>In vitro</i> skin penetration depth.....	137
3.3.10	<i>In vitro</i> MN dissolution in the skin.....	139
3.3.11	Drug content and distribution.....	139
3.3.12	<i>In vitro</i> drug release study.....	141
3.3.13	<i>In vitro</i> drug permeation and mass balance studies.....	145
3.4	Conclusion.....	148

CHAPTER 4 LOADING A HYDROPHOBIC MODEL DRUG INTO RICE STARCH-BASED MICRONEEDLES	150
4.1 Introduction.....	150
4.2 Materials and methods	152
4.2.1 Materials	152
4.2.2 HPLC	152
4.2.3 Formulation of KTP-loaded RSC-based MN arrays.....	152
4.2.4 Homogeneity of matrix and drug distribution of PVA20K5 and PVP40K5 films	153
4.2.5 Characterisation of KTP-loaded RSC-based MN arrays	153
4.2.5(a) Determination of MN shape and geometry.....	153
4.2.5(a)(i) Optical microscopy.....	153
4.2.5(a)(ii) SEM.....	154
4.2.5(b) ATR-FTIR spectroscopy.....	154
4.2.5(c) DSC.....	154
4.2.5(d) Mechanical studies.....	155
4.2.5(d)(i) MN %compression test.....	155
4.2.5(d)(ii) Axial compression test.....	155
4.2.5(e) MN insertion.....	155
4.2.5(e)(i) Parafilm [®] insertion study.....	155
4.2.5(e)(ii) <i>In vitro</i> insertion in porcine skin.....	155
4.2.5(f) <i>In vitro</i> MN dissolution in the skin.....	156
4.2.5(g) Drug content and distribution	156
4.2.5(h) <i>In vitro</i> drug release study	156
4.2.5(i) <i>In vitro</i> permeation and mass balance studies	156
4.2.6 Statistical analysis.....	157
4.3 Results and discussion	157
4.3.1 KTP distribution in PVA20K5 and PVP40K5 films	157

4.3.2	Characterisation of PVA20K5-MN and PVP40K5-MN.....	161
4.3.2(a)	MN shape and geometry	161
4.3.2(b)	ATR-FTIR spectroscopy.....	163
4.3.2(c)	DSC.....	169
4.3.2(d)	Mechanical studies.....	174
4.3.2(e)	<i>In vitro</i> MN insertion studies	176
4.3.2(f)	<i>In vitro</i> MN dissolution in the skin.....	180
4.3.2(g)	Drug content and distribution	181
4.3.2(h)	<i>In vitro</i> drug release study	182
4.3.2(i)	<i>In vitro</i> drug permeation and mass balance studies	186
4.4	Conclusions.....	191
CHAPTER 5 STABILITY OF RICE STARCH-BASED MICRONEEDLES UNDER DIFFERENT HUMIDITY CONDITIONS 193		
5.1	Introduction.....	193
5.2	Materials and methods	194
5.2.1	Formulation and storage conditions of RSC-based MNs and films	194
5.2.2	Determination of water content of MNs	195
5.2.3	Determination of MN shape and geometry.....	195
5.2.4	ATR-FTIR spectroscopy.....	196
5.2.5	Parafilm [®] insertion study	196
5.2.6	Mechanical studies.....	196
5.2.6(a)	MN %compression test.....	196
5.2.6(b)	Axial compression test.....	197
5.2.7	Drug content and distribution	197
5.2.8	Statistical analysis.....	197
5.3	Results and discussion	197
5.3.1	ATR-FTIR spectroscopy.....	197

5.3.2	Drug content and distribution	209
5.3.3	Morphology and colour change	211
5.3.4	Mechanical studies	219
5.3.5	Parafilm [®] insertion study	223
5.4	Conclusions	230
CHAPTER 6 CONCLUSIONS AND FUTURE WORK		233
6.1	Conclusions	233
6.2	Future work	237
REFERENCES		239

LIST OF TABLES

		Page
Table 1.1	Physicochemical properties of PVP. Adapted from Kurakula and Rao (2020).	17
Table 1.2	Physicochemical properties of PVA. Adapted from Brough et al. (2016).....	19
Table 1.3	RSC-based formulations for drug delivery.....	28
Table 1.4	Physicochemical properties of LID	32
Table 1.5	Physicochemical properties of KTP	35
Table 2.1	Coding system and quantities of RSC, PVP, PVA and sorbitol used in the preparation of each formulation (total solid concentration =10 % w/v).....	44
Table 2.2	T_g and T_m of RSC powder, PVA powder, PVP powder, and all RSC-based films (mean \pm SD, n = 2).....	65
Table 2.3	Mechanical properties of RSC-based films (mean \pm SD, n = 3).....	70
Table 2.4	Geometry information of different RSC-based MNs (mean \pm SD, n = 30)	76
Table 2.5	Spearman's correlation coefficient between the %compression of MN and different mechanical parameters of films.....	86
Table 2.6	Rule of thumb for interpretation of correlation coefficient. Adapted from Hinkle et al. (2003).....	87
Table 2.7	Pearson correlation coefficient between the dissolution of films and corresponding MNs	88
Table 2.8	T_g and T_m of films and MNs of RSC100, PVA100, PVP100 (mean \pm SD, n = 2)	92
Table 3.1	Formulations of selected commercially available LID products	108
Table 3.2	Geometry information of blank and LID-loaded MN arrays (mean \pm SD, n = 30)	118
Table 3.3	Thermal events of LID-loaded physical mixtures and MNs (mean \pm SD, n = 2)	135

Table 3.4	LID distribution in PVA20L10-MN and PVP40L10-MN arrays (mean \pm SD, n = 5).....	140
Table 3.5	r^2 values of LID release kinetic models from PVA20L10-MN and PVP40L10-MN	142
Table 3.6	Interpretation of the Korsmeyer-Peppas exponent for cylindrical samples. Adapted from Fosca et al. (2022).	143
Table 4.1	KTP content of PVA20K5-F and PVP40K5-F (mean \pm SD, n = 10).....	160
Table 4.2	Geometry information of blank and KTP-loaded MN arrays (mean \pm SD, n = 3)	161
Table 4.3	Thermal events of KTP-loaded PMs and MNs (mean \pm SD, n = 2).....	174
Table 4.4	KTP distribution in PVA20K5-MN and PVP40K5-MN arrays (mean \pm SD, n = 5).....	181
Table 4.5	r^2 values of KTP release kinetic models from PVA20K5-MN and PVP40K5-MN	185
Table 5.1	Absorbance ratio of 1047/1016 cm^{-1} bands ($I_{1047/1016}$) for the FTIR spectrum of RSC100-F stored under the dry and humid conditions for 6 months (mean \pm SD, n = 3)	201
Table 5.2	Water content of PVA20L10-MN, PVP40L10-MN, PVA20K5-MN, and PVP40K5-MN after storing for 6 months under dry and humid conditions (mean \pm SD, n = 3)	209
Table 5.3	Total drug content of MNs after storage under dry and humid conditions for 6 months (mean \pm SD, n = 5)	210
Table 5.4	Amount of drug localised in the MNs after storage under a dry condition for 6 months (mean \pm SD, n = 5)	210
Table 5.5	Geometry information of LID- and KTP-loaded MNs after storing for 6 months under a dry condition (mean \pm SD, n = 30).....	213
Table 5.6	Geometry information of LID- and KTP-loaded MNs after storing for 1 month under a humid condition (mean \pm SD, n = 30).....	217

LIST OF FIGURES

		Page
Figure 1.1	Cross-section illustration showing the main components of human skin. Adapted from Azmana et al. (2020).....	3
Figure 1.2	MN penetration across the SC. Adapted from Azmana et al. (2020).....	7
Figure 1.3	Total number of publications on MNs and polymeric MNs over the past 20 years. Adapted from Yadav et al. (2021).....	9
Figure 1.4	Illustrations of the design of (A) solid, (B) coated, (C) hollow, (D) hydrogel-forming, and (E) dissolving MNs. Adapted from Larraneta et al. (2016).....	10
Figure 1.5	Examples of methods commonly used for dissolving MNs fabrication including (A) casting, (B) atomised spraying, (C) droplet-born air blowing, and (D) three-dimensional printing. Adapted from Sartawi et al. (2022).....	15
Figure 1.6	Structure of amylose and amylopectin. Adapted from Willfahrt et al. (2019).....	23
Figure 1.7	Illustration of starch gelatinisation and retrogradation. Adapted from del Carmen Robles-Ramírez et al. (2012).....	24
Figure 1.8	(A) Dry rice paper and (B) its application of soaked rice paper as a facial mask. Adapted from Maarouf et al. (2018).	30
Figure 2.1	(A) Determination of mechanical properties of films using Texture Analyser (d = radius of the rice starch film in the sample holder opening (initial length); a = initial length – radius of probe; b = displacement of the probe; $c + r$ = length after strain; c = length of a after strain; and r = radius of probe). (B) Typical plot of force versus displacement for films subjected to puncture (F is the force required to puncture the film, and b is the distance at break).	47
Figure 2.2	Illustration of RSC-based MN array formulation by double casting technique	49
Figure 2.3	The area of MNs (A) before and (B) after insertion into gelatine block measured by CellSens [®] Imaging software	55
Figure 2.4	Digital images of films of (A) plasticised and (B) unplasticised RSC-blended films.....	58
Figure 2.5	FTIR spectra of (A) RSC, (B) PVP, and (C) PVA powders	60

Figure 2.6	FTIR spectra of RSC100, PVP100, and RSC-PVP films.....	62
Figure 2.7	FTIR spectra of RSC100, PVA100, and RSC-PVA films	63
Figure 2.8	DSC thermograms showing the (A) first and (B) second heating cycles of RSC, PVA and PVP powders.....	64
Figure 2.9	DSC thermograms showing the (A) first and (B) second heating cycles of RSC100, PVA100, and RSC-PVA films.....	66
Figure 2.10	DSC thermograms showing the (A) first and (B) second heating cycles of RSC100, PVP100, and RSC-PVP films	69
Figure 2.11	Dissolution percentage of RSC-blended films after 24 h (mean \pm SD, n = 5)	73
Figure 2.12	The top view of the PDMS moulds used for RSC-based MN arrays	75
Figure 2.13	Microscopic image of different MNs (magnification: 6.3 \times , scale: 100 μ m)	75
Figure 2.14	Microscopic images of RSC-based MNs before and after performing the %compression test (magnification: 6.3 \times , scale: 100 μ m)	79
Figure 2.15	%compression of RSC-based MN arrays (mean \pm SD, n = 3), (* indicates significant difference, p < 0.05, Kruskal-Wallis)	80
Figure 2.16	Digital image of the holes created in each Parafilm [®] layer after the application of (A) PVP100-MN, and (B) RSC100-MN using Texture Analyser	81
Figure 2.17	Percentage of holes created in Parafilm [®] layers after the insertion of (A) PVP- and (B) PVA-blended MNs (mean \pm SD, n = 3)	82
Figure 2.18	Dissolution of RSC-based MN arrays blended with (A) PVA or (B) PVP into gelatine block (mean \pm SD, n = 5).....	84
Figure 2.19	Dissolution % of PVA and PVP blended RSC films after 1 min (mean \pm SD, n = 5)	88
Figure 2.20	FTIR spectra of films and MNs of (A) RSC100, (B) PVA100, (C) PVP100, (D) PVA20, and (E) PVP40.....	89
Figure 2.21	DSC thermograms showing the (A) first heating and (B) second heating cycles of films and MNs for RSC100, PVA100, PVP100, PVA20, and PVP40.....	91

Figure 2.22	SEM micrographs of (A) RSC100-MN, (B) PVA20-MN, (C) PVP40-MN, and (D) PVP100-MN (magnification: $\times 100$)	93
Figure 2.23	SEM micrographs of (A) RSC100-MN, (B) PVA20-MN, (C) PVP40-MN, and (D) PVP100-MN (magnification: $\times 400$)	94
Figure 2.24	SEM micrographs of (A) RSC100-MN, (B) PVA20-MN, (C) PVP40-MN, and (D) PVP100-MN (magnification: $\times 2000$)	95
Figure 2.25	FTIR spectra of (A) PVA powder, (B) RSC powder, (C) PVA20 physical mixture, and (D) PVA20-MN	96
Figure 2.26	FTIR spectra of (A) RSC powder, (B) PVP powder, (C) PVP40 physical mixture and (D) PVP40-MN.....	97
Figure 2.27	Force-displacement curves of RSC100-MN, PVA20-MN, PVP40-MN, and PVP100-MN in axial compression test.....	99
Figure 2.28	Insertion site for (A) RSC100-MN, (B) PVP40-MN, (C) PVA20-MN, and (D) PVP100-MN into porcine ear skin that was stained with methylene blue	102
Figure 2.29	MN insertion ratio into porcine ear skin (mean \pm SD, n = 20)	102
Figure 2.30	(A) Cross-sectioned view of untreated porcine skin and porcine skin treated with (B) PVA20-MN, (C) PVP40-MN, and (D) PVP100-MN (stained with haematoxylin and eosin; scale: 100 μ m)	104
Figure 2.31	Microscopic images of MNs after insertion into excised porcine skin at different times (magnification: 6.3 \times , scale: 100 μ m)	105
Figure 3.1	Microscopic image of blank and LID loaded MNs (magnification: 6.3 \times , scale: 100 μ m)	117
Figure 3.2	%compression of blank and LID-loaded MN arrays (mean \pm SD, n = 3), (* indicates significant difference as compared with the corresponding blank MN, $p < 0.05$, Kruskal-Wallis)	119
Figure 3.3	Percentage of holes created in Parafilm [®] layers after the insertion of blank and LID-loaded MN arrays of (A) PVA20 and (B) PVP40 (mean \pm SD, n = 3).....	121
Figure 3.4	Insertion site of (A) PVA20L5-MN, (B) PVP40L5-MN, (C) PVA20L10-MN, (D) PVP40L10-MN, (E) PVA20L15-MN, and (F) PVP40L15-MN into porcine ear skin stained with methylene blue.....	123

Figure 3.5	SEM images of (A) PVA20L10-MN and (B) PVP40L10-MN (magnification: $\times 100$)	124
Figure 3.6	SEM images of (A) PVA20L10-MN and (B) PVP40L10-MN (magnification: $\times 400$)	125
Figure 3.7	SEM images of the tip of (A) PVA20L10-MN and (B) PVP40L10-MN (magnification: $\times 2000$)	125
Figure 3.8	FTIR spectra of LID powder	126
Figure 3.9	FTIR spectra of PVA20L10-MN, PVA20-MN, PVA20L10-PM, and PVA20-PM.....	128
Figure 3.10	FTIR spectra of PVP40L10-MN, PVP40-MN, PVP40L10-PM, and PVP40-PM	130
Figure 3.11	DSC thermograms showing the (A) first and (B) second heating cycles of LID powder	131
Figure 3.12	DSC thermograms showing the (A) first and (B) second heating cycles of PVA20L10-PM, PVA20-MN, and PVA20L10-MN.....	132
Figure 3.13	DSC thermograms showing the (A) first and (B) second heating cycles of PVP40L10-PM, PVP40-MN, and PVP40L10-MN.....	133
Figure 3.14	Force-displacement curves of PVA20-MN, PVP40-MN, PVA20L10-MN, and PVP40L10-MN in the axial compression test	136
Figure 3.15	(A) Cross-sectioned view of untreated porcine skin and porcine skin treated with (B) PVA20L10-MN, and (C) PVP40L10-MN (stained with haematoxylin and eosin; scale: 100 μm)	137
Figure 3.16	Microscopic images of LID-loaded MNs after insertion into excised porcine skin over 60 min (magnification: 6.3 \times , scale: 100 μm)	139
Figure 3.17	(A) Digital photo of PVA20L10-MN and (B) an illustration of the MN array parts.....	140
Figure 3.18	<i>In vitro</i> cumulative amount of LID released from PVA20L10-MN and PVP40L10-MN over (A) 60 min and (B) 24 h (mean \pm SD, n = 3).....	141
Figure 3.19	Mechanism of drug release from dissolving MN	144
Figure 3.20	<i>In vitro</i> percentage of cumulative amount of LID permeated across full-thickness porcine ear skin from LID solution,	

	PVA20L10-C, PVA20L10-MN, PVP40L10-C, and PVP40L10-MN (mean \pm SD, n = 3).....	146
Figure 3.21	Mass balance study for different LID-loaded formulations (n = 3, mean \pm SD).....	148
Figure 4.1	Visual appearance of PVA20K5-F and PVP40K5-F	159
Figure 4.2	Microscopic images of (A and C) PVA20K5-F and (B and D) PVP40K5-F investigated (A and B) without and (C and D) with polarised mode (magnification: 6.3 \times).....	159
Figure 4.3	SEM micrographs of (A) PVA20K5-MN and (B) PVP40K5-MN (magnification: \times 100)	162
Figure 4.4	SEM micrographs of (A) PVA20K5-MN and (B) PVP40K5-MN (magnification: \times 400)	162
Figure 4.5	SEM micrographs of (A) PVA20K5-MN and (B) PVP40K5-MN (magnification: \times 2000)	163
Figure 4.6	FTIR spectrum of KTP powder.....	164
Figure 4.7	FTIR spectra of PVA20-PM, PVA20K5PM, PVA20-MN, and PVA20K5-MN.....	165
Figure 4.8	FTIR spectra of PVA20K5-PM and PVA20K5-MN from 1900 to 600 cm^{-1}	167
Figure 4.9	FTIR spectra of PVP40-PM, PVP40K5-PM, PVP40-MN, and PVP40K5-MN	168
Figure 4.10	FTIR spectra of PVP40K5-PM and PVP40K5-MN from 1900 to 600 cm^{-1}	169
Figure 4.11	DSC thermograms showing the (A) first and (B) second heating cycles of KTP powder.....	170
Figure 4.12	DSC thermograms showing the first heating cycle of PVA20K5-PM, PVA20K5-MN, PVP40K5-PM, and PVP40K5-MN	171
Figure 4.13	DSC thermograms showing the second heating cycle of PVA20K5-PM, PVA20K5-MN, PVP40K5-PM, and PVP40K5-MN	172
Figure 4.14	%compression of blank and KTP-loaded MNs (mean \pm SD, n = 3).....	175
Figure 4.15	Force-displacement curves of PVA20-MN, PVP40-MN, PVA20K5-MN, and PVP40K5-MN in the axial compression test.....	176

Figure 4.16	Percentage of holes created in Parafilm [®] layers after the insertion of PVA20-MN, PVA20K5-MN, PVP40-MN, and PVP40K5-MN (mean \pm SD, n = 3)	177
Figure 4.17	Insertion site of (A) PVA20K5-MN and (B) PVP40K5-MN into porcine ear skin stained with methylene blue	178
Figure 4.18	Insertion ratio of blank and KTP-loaded MNs into porcine ear skin (mean \pm SD, n = 20).....	178
Figure 4.19	(A) Cross-sectioned view of untreated porcine skin and porcine skin treated with (B) PVA20K5-MN, and (C) PVP40K5-MN (stained with haematoxylin and eosin; scale: 100 μ m)	179
Figure 4.20	Microscopic images of KTP-loaded MNs after insertion into excised porcine ear skin over 60 min (magnification: 6.3 \times , scale: 100 μ m)	180
Figure 4.21	<i>In vitro</i> cumulative amount of KTP released from PVA20K5-MN and PVP40K5-MN over (A) 2 and (B) 24 h (mean \pm SD, n = 3)	183
Figure 4.22	<i>In vitro</i> percentage of cumulative amount of KTP permeated across full-thickness porcine ear skin from KTP solution, PVA20K5-C, PVA20K5-MN, PVP40K5-C, and PVP40K5-MN (mean \pm SD, n = 3).....	187
Figure 4.23	Mass balance study for different KTP-loaded formulations (mean \pm SD, n = 3)	189
Figure 5.1	FTIR spectra of RSC100-F after storing under (A) dry and (B) humid conditions for 6 months.....	199
Figure 5.2	FTIR spectra of PVA20L10-MN after storage under (A) dry and (B) humid conditions for 6 months.....	202
Figure 5.3	FTIR spectra of PVA20K5-MN after storing under (A) dry and (B) humid conditions for 6 months.....	203
Figure 5.4	FTIR spectra of PVP40L10-MN after storing under (A) dry and (B) humid conditions for 6 months.....	205
Figure 5.5	FTIR spectra of PVP40K5-MN after storing under (A) dry and (B) humid conditions for 6 months.....	206
Figure 5.6	Digital images of PVA20L10-MN, PVP40L10-MN, PVA20K5-MN, and PVP40K5-MN after storing under a dry condition for 6 months.....	211
Figure 5.7	Microscopic images of PVA20L10-MN, PVP40L10-MN, PVA20K5-MN, and PVP40K5-MN after storing under a dry	

	condition for 6 months (magnification: 6.3×, scale: 100 μm)	212
Figure 5.8	Digital images of films after storing under a dry condition for 6 months.....	214
Figure 5.9	Digital images of PVA20L10-MN, PVP40L10-MN, PVA20K5-MN, and PVP40K5-MN after storing under a humid condition for 1 month.....	215
Figure 5.10	Digital images of films after storing under a humid condition for 6 months.....	215
Figure 5.11	Microscopic images of PVA20L10-MN, PVP40L10-MN, PVA20K5-MN, and PVP40K5-MN after storing under a humid condition for 1 month (magnification: 6.3×, scale: 100 μm)	217
Figure 5.12	Force-displacement curves of (A) PVA20L10-MN, (B) PVP40L10-MN, (C) PVA20K5-MN and (D) PVP40K5-MN after storage under a dry condition for 6 months.....	221
Figure 5.13	%compression of (A) LID- and (B) KTP-loaded MNs after storage under a dry condition for 6 months (mean ± SD, n = 3).....	222
Figure 5.14	Microscopic images of (A) PVA20L10-MN, (B) PVP40L10-MN, (C) PVA20K5-MN, and (D) PVP40K5-MN stored under a humid condition for 1 month after the %compression test (magnification: 6.3 ×).....	223
Figure 5.15	Percentage of holes created in Parafilm® layers after the insertion of (A) PVA20L10-MN, (B) PVP40L10-MN, (C) PVA20K5-MN, and (D) PVP40K5-MN after storage under a dry condition for 6 months (mean ± SD, n = 3).....	225
Figure 5.16	%compression of the MN after performing the MN %compression test on (A) LID- and (B) KTP-loaded MNs after storage under a humid condition up to 10 min (mean ± SD, n = 3), (* indicates significant difference as compared with the corresponding blank MN, <i>p</i> < 0.05, ANOVA).....	227
Figure 5.17	Percentage of holes created in Parafilm® layers after the insertion of (A) PVA20L10-MN, (B) PVP40L10-MN, (C) PVA20K5-MN, and (D) PVP40K5-MN after storage under a humid condition up to 10 min (mean ± SD, n = 3).....	228

LIST OF SYMBOLS

%	Percentage
×	Magnification
°C	Degree Celsius
L	Litter
M	Molarity
m ²	Meter square
cm ²	Centimetre square
mL	Millilitre
mm	Millimetre
N	Newton
nm	nanometre
r^2	the coefficient of determination
rpm	Round per minute
w/v	Weight/volume
w/w	Weight/ weight
Da	Dalton
RCF	Relative centrifugal force

LIST OF ABBREVIATIONS

RSC	Rice starch
MN	Microneedle
SC	Stratum corneum
ANOVA	Analysis of variance
DSC	Differential scanning calorimetry
ATR-FTIR	Attenuated total reflectance-fourier transform infrared
PS	Puncture strength
EP	Energy to puncture
EB	Elongation to break
HPLC	High-performance liquid chromatography
MW	Molecular weight
PBS	Phosphate buffer saline
PVA	Polyvinyl alcohol
PVP	Polyvinyl pyrrolidone
HPMC	Hydroxypropyl methyl cellulose
CMC	Carboxy methyl cellulose
SD	Standard deviation
SEM	Scanning electron microscopy
T_g	Glass transition temperature
T_m	Melting point
EtOH	Ethanol
NSAID	Non-steroidal anti-inflammatory drug
FDA	Food and Drug Administration
US	United States

UK	United Kingdom
IUPAC	International union of pure and applied chemistry
ICH	International Council for Harmonisation

LIST OF APPENDICES

- Appendix A Selection of plasticiser and polymer for RSC-based MN formulation
- Appendix B Selection of polymer for MN base-plate formulation
- Appendix C HPLC method development and validation for LID and KTP
- Appendix D Selection of a cosolvent system for the development of KTP-loaded MNs

PEMBANGUNAN JARUM MIKRO KANJI BERAS UNTUK PENYAMPAIAN UBAT KE KULIT

ABSTRAK

Jarum mikro (MN) merupakan peranti bioperubatan invasif minimal yang membantu ubat-ubatan melepasi halangan kulit, yang menghasilkan kesan farmakologi sistemik dan terlokalisasi. MN larut dapat dikaitkan dengan pematuhan pesakit yang tinggi dan risiko pencemaran silang yang lebih rendah berbanding dengan jenis MN yang lain. Kanji beras (RSC) mempunyai potensi yang tinggi untuk digunakan dalam pembangunan MN larut kerana dengan ciri-ciri pembentukan filem yang baik, kebolehuraian biodegradasi, ketoksikan yang rendah, dan kos yang rendah. Walau bagaimanapun, formulasi MN larut menggunakan RSC merupakan cabaran disebabkan oleh sifat kerapuhan yang ada pada RSC. Tesis ini bertujuan untuk meneroka RSC sebagai biopolimer untuk pembuatan MN larut untuk penyampaian ubat ke kulit. Formulasi MN larut dengan RSC tunggal adalah mustahil disebabkan oleh sifat mekanikal RSC yang lemah. Oleh itu, campuran polimer RSC dengan polivinil alkohol (PVA) atau polivinil pirrolidon (PVP) telah digunakan sebagai langkah awal untuk membangunkan filem sebelum pembangunan MN. Penambahan PVA atau PVP dapat meningkatkan kekuatan mekanikal dan kelarutan filem berasaskan RSC. Sementara itu, pencirian campuran RSC yang berbeza menunjukkan bahawa MN larut yang diformulasikan dengan campuran RSC menggunakan 20% w/w PVA (PVA20-MN) atau 40% w/w PVP (PVP40-MN) menunjukkan pembentukan jarum yang utuh dengan kekuatan mekanikal yang mencukupi, penembusan kulit, dan pelarutan dalam masa 60 minit. Didapati bahawa filem dan MN

berdasarkan RSC mempunyai struktur kimia dan kekuatan mekanikal yang sama. Pelarutan filem dan MN juga mempunyai korelasi yang tinggi. Ini dapat membantu dalam meramalkan sifat MN dengan prosedur penyiasatan yang lebih mudah melalui filem yang berkaitan. PVA20-MN dan PVP40-MN dikaji lebih lanjut sebagai platform untuk penyampaian lidokain hidroklorida (LID) sebagai ubat model hidrofilik ke kulit. MN mengandungi LID (10 % w/w) mempunyai geometri dan kekuatan MN yang seragam dan dapat menembusi kulit telinga khinzir dengan sempurna. Selain itu, peresapan *in vitro* melalui kulit telinga khinzir menunjukkan bahawa sebanyak ~ 53% LID diresapkan selepas 24 jam penggunaan MN yang mengandungi LID. Ini adalah > 3 kali ganda berbanding dengan MN bengkok (~ 13%) dan larutan LID (~ 16%). Pemuatan ubat hidrofobik ke dalam matriks hidrofilik merupakan satu cabaran. Walau bagaimanapun, kajian ini menunjukkan bahawa ketoprofen (KTP) (5% w/w) berjaya dilarutkan dan ditaburkan secara seragam dalam matriks hidrofilik PVA20-MN dan PVP40-MN dengan menggunakan sistem pelarut bersama etanol/air yang mudah. Kedua-dua MN yang mengandungi KTP adalah tajam dan kuat untuk penembusan kulit. Selain itu, peresapan *in vitro* menunjukkan bahawa jumlah KTP yang diresapkan melalui kulit telinga khinzir dengan penggunaan MN yang mengandungi KTP (~ 37%) meningkat sebanyak > 2 - 5 kali ganda berbanding dengan MN bengkok (~ 7%) dan larutan KTP (~ 16%). Kestabilan MN berdasarkan RSC dalam keadaan kering dan lembap juga disiasat secara terperinci. Semua MN adalah stabil dalam keadaan penyimpanan kering (kelembapan relatif: $2 \pm 2\%$ pada suhu bilik) selama 6 bulan. Sebaliknya, apabila terdedah kepada keadaan dengan kelembapan yang tinggi (kelembapan relatif: $75 \pm 2\%$ pada suhu $40\text{ }^{\circ}\text{C}$), semua MN berdasarkan RSC kehilangan kestabilan kimia, kekuatan mekanikal, dan keupayaan penembusan. Oleh itu, ia disarankan untuk menyimpan MN berdasarkan RSC dalam balang vakum atau

pengering vakum. Selain itu, MN harus diaplikasikan ke kulit dalam masa 2 menit setelah dibuka untuk memastikan penembusan kulit yang efisien. Kesimpulannya, MN larut berjaya diformulasikan dengan menggunakan campuran RSC dengan PVA atau PVP. Selain itu, MN berasaskan RSC mampu menyampaikan ubat model yang bersifat hidrofilik (LID) dan hidrofobik (KTP) ke kulit dengan peningkatan peresapan kulit. MN berasaskan RSC dapat digunakan sebagai platform penyampaian ubat ke kulit.

DEVELOPMENT OF RICE STARCH MICRONEEDLES FOR DRUG DELIVERY TO THE SKIN

ABSTRACT

Microneedles (MNs) are minimally invasive biomedical devices that help drugs to bypass the skin barrier, resulting in systemic and localised pharmacological effects. Dissolving MNs are associated with high patient compliance and lower cross-contamination risk as compared to other MN types. Rice starch (RSC) has a high potential to be used in the development of dissolving MNs owing to its good film-forming properties, biodegradability, non-toxicity, and low cost. However, formulation of dissolving MNs using RSC is challenging due to the inherent brittleness of RSC. This thesis aims to explore RSC as a biopolymer for the fabrication of dissolving MN for drug delivery to the skin. Formulation of dissolving MNs with neat RSC was impossible due to the poor mechanical properties of RSC. Therefore, polymer blends of RSC with polyvinyl alcohol (PVA) or polyvinyl pyrrolidone (PVP) were initially used to develop films as a preliminary investigation before MN development. The addition of PVA or PVP enhanced the mechanical strength and dissolution of RSC-based films. Meanwhile, characterisation of different RSC blends demonstrated that MNs formulated with RSC blends using 20 % w/w of PVA (PVA20-MN) or 40 % w/w of PVP (PVP40-MN) showed intact needle formation with sufficient mechanical strength, skin insertion and dissolution within 60 min. It was shown that RSC-based films and MNs have identical chemical structure and mechanical strength. The dissolution of films and MNs were also highly correlated. This can be helpful in the prediction of the properties of MNs by a simpler investigational procedure of the

corresponding films. PVA20-MN and PVP40-MN were further investigated as a platform for delivering lidocaine hydrochloride (LID) as a hydrophilic model drug to the skin. LID-loaded MNs (10 %w/w) possessed uniform MN geometry and strength and were able to completely penetrate porcine ear skin. Moreover, *in vitro* permeation through porcine ear skin showed that ~ 53 % of LID permeated after 24 h of LID-loaded MN application. This was > 3-fold higher as compared with bent MNs (~ 13 %) and a LID solution (~ 16 %). Loading a hydrophobic drug into a hydrophilic matrix is challenging. However, this work showed that ketoprofen (KTP) (5 %w/w) was successfully dissolved and uniformly distributed within the hydrophilic matrix of PVA20-MN and PVP40-MN using a simple ethanol/ water cosolvent system. Both KTP-loaded MNs were sharp and strong enough for skin insertion. In addition, *in vitro* permeation showed that the amount of KTP permeated through porcine ear skin with the application of KTP-loaded MNs (~ 37 %) increased by > 2 – 5 folds as compared to bent MNs (~ 7 %) and a KTP solution (~ 16 %). The stability of RSC-based MNs under dry and humid conditions was thoroughly investigated. All MNs were stable under a dry storage condition (relative humidity: 2 ± 2 % at room temperature) for 6 months. On the contrary, when exposed to a high humid condition (relative humidity: 75 ± 2 % at 40 °C), all RSC-based MNs lost their chemical stability, mechanical strength, and insertion ability. As a result, it is recommended to store RSC-based MNs in a vacuum or desiccant-sealed container. Furthermore, the MNs should be applied to the skin within 2 min after unpacking to ensure an efficient skin insertion. In conclusion, dissolving MNs were successfully formulated using RSC blends with PVA or PVP. In addition, RSC-based MNs were able to deliver both hydrophilic (LID) and hydrophobic (KTP) model drugs to the skin with enhanced skin permeation. RSC-based MNs can be employed as a platform for drug delivery to the skin.

CHAPTER 1

INTRODUCTION

1.1 Overview

Skin has been employed as a route of drug administration for treating a wide range of illnesses. The administration of drugs to the skin provides high patient compliance and avoids gastrointestinal degradation as well as hepatic first-pass metabolism as compared with the oral route (Joshi et al., 2014; Singhvi et al., 2019). However, drug permeation through the skin is limited by the excellent barrier properties of the skin's outermost layer, the stratum corneum (SC) (Haque & Talukder, 2018). Therefore, many strategies have been employed to enhance drug permeation through the SC such as eutectic systems, vesicles, chemical enhancers, ultrasound, iontophoresis and microneedles (MNs) (Azagury et al., 2014; Damiri et al., 2022; Gratieri & Kalia, 2013; Han & Das, 2015; Lademann et al., 2009; Yu et al., 2021; Zaid Alkilani et al., 2015; Zhang et al., 2022).

MN array is composed of micron-sized needles (usually 150 – 1500 μm in length). MNs provide a mean of delivering a wide variety of pharmaceutical agents across the skin in a minimally invasive and virtually painless manner as compared with hypodermic injections (Vandervoort & Ludwig, 2008; Waghule et al., 2019). Recently, dissolving MNs attract significant attention from researchers owing to their safety, cost-effectiveness, and high patient compliance as compared with other MN types (Sartawi et al., 2022). Dissolving MNs can be fabricated with biocompatible hydrophilic polymers from natural sources such as sodium chondroitin sulfate, dextran, gelatine, chitin, silk, chitosan, and starch (Larraneta et al., 2016).

Starch is a biodegradable, cheap, abundant, and non-toxic biopolymer with good film-forming ability. These outstanding properties, especially the excellent film-forming ability, make starch an attractive biopolymer for MN fabrication. Among the different sources of starch, starch obtained from rice has a small granular size, high paste stability, superior acid resistance, low allergenicity, and is available in different ratios of amylose and amylopectin (Gayin, 2015; Lawal et al., 2011). In addition, rice starch (RSC) has been previously investigated as a material for developing films for packaging and drug delivery (Alrimawi et al., 2021; Marichelvam et al., 2019). Thus, RSC is explored here as a potential polymer for MN formulation.

Despite its exceptional properties, RSC is not given enough attention as a carrier for drug delivery to the skin, especially as MNs. Therefore, this thesis aims to formulate dissolving MNs from RSC and to investigate the RSC-based MNs as a platform for delivering hydrophilic and hydrophobic model drugs to the skin.

1.2 Skin

1.2.1 Skin structure

Skin is the largest organ, covering a surface area of roughly 1.7 m² in an average adult and comprising about 10 % of total body mass (Arens & Zhang, 2006; Joshi et al., 2014). The thickness of human skin is ~ 3 mm and varies according to health, age, and the site of the body (being thickest at the soles of the feet and thinnest at the eyelids) (Mehta, 2004). Our skin performs a variety of body functions such as safeguarding against harmful environmental chemicals and microorganisms, blocking ultraviolet (UV) radiation, controlling body temperature, producing vitamin D (cholecalciferol), and retaining bodily fluids (Kolarsick et al., 2011; Menon, 2002).

Human skin consists of three distinct layers: the epidermis, dermis, and hypodermis (Figure 1.1).

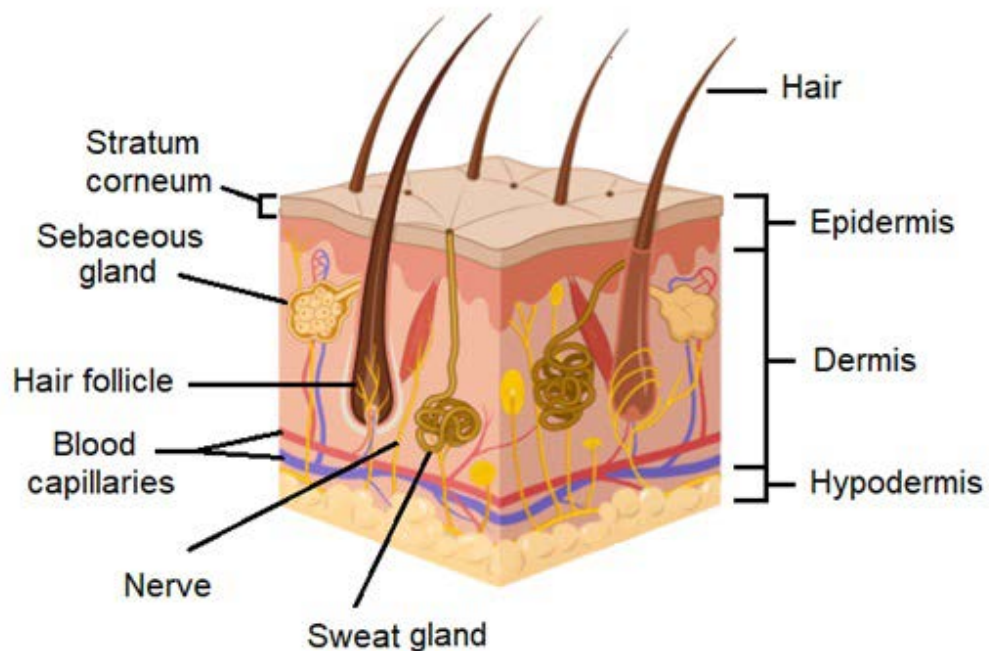


Figure 1.1 Cross-section illustration showing the main components of human skin. Adapted from Azmana et al. (2020).

The epidermis (thickness: $\sim 100 \mu\text{m}$) comprises five distinct sub-layers: the SC, stratum lucidum, stratum granulosum, stratum spinosum, and stratum basal. The SC (thickness: $\sim 10 - 20 \mu\text{m}$) is the outermost layer of the epidermis and is composed of a highly dense (roughly 1.4 g/cm^3) matrix of well-arranged corneocytes and lipids. Therefore, the SC acts as a mechanical barrier to protect the lower sub-layers of the epidermis from water loss and foreign materials and is considered the main skin barrier for medication absorption (Haque & Talukder, 2018; Kolarsick et al., 2011).

The other four sub-layers of the epidermis (stratum lucidum, stratum granulosum, stratum spinosum, and stratum basal) are collectively called the viable

epidermis (Bouwstra et al., 2003; Hadgraft, 2004). The thickness of the viable epidermis is approximately between 0.06 – 0.8 mm (Patel et al., 2021).

The dermis is a fibrous layer of connective tissue (thickness: ~ 1 – 3 mm) located directly under the epidermis endings (Bouwstra et al., 2003). The dermis accounts for ~ 90 % of the total skin mass, and its structure consists of a matrix of loose connective tissue mainly formed of fibrous proteins collagen and elastin (Jablonski, 2008). In addition, hair follicles, sebaceous and sweat glands, and a network of capillaries, lymphatic veins, and nerve endings are located in the deep part of the dermis (Vandervoort & Ludwig, 2008; Walters & Roberts, 2002). The dermis provides protection to the body from mechanical injury and helps with thermal regulation (Kolarsick et al., 2011).

The subcutaneous layer is the innermost layer of the skin located directly below the dermis. The subcutaneous layer is composed of fat and loose, fibrous, white connective tissue. The subcutaneous layer serves as shock absorber, heat insulator, and energy reservoir for the body (Walters & Roberts, 2002).

1.2.2 Dermal drug delivery

The application of medicinal substances to the skin has been used to cure various disorders for thousands of years (Benson & Watkinson, 2012). Nowadays, a variety of local and systemic disorders such as pain management, local infections, smoking cessation, hormone deficiency, motion sickness, and cardiovascular disorders, are treated by topical and transdermal drug delivery (Goossens & Gonçalo, 2020; Mehta, 2004; Narasimha Murthy & Shivakumar, 2010). Topical drug delivery is primarily designed for local effects, while transdermal drug delivery is intended

when a systemic effect is desired (Arens & Zhang, 2006; Joshi et al., 2014; Tanwar & Sachdeva, 2016).

The delivery of medications through the skin has many benefits as compared with the oral route, including the avoidance of gastric acid and enzymes, pH fluctuation through the gastrointestinal tract, and most importantly, the avoidance of the hepatic first pass metabolism (Benson & Watkinson, 2012). In addition, the dermal route is non-invasive and allows better patient convenience and drug delivery control than the parenteral route (Davidson et al., 2008).

However, dermal drug delivery is limited due to the SC, which is considered the main barrier of the skin that restricts the penetration of any topically applied compounds (Wermeling et al., 2008). The SC is composed of highly organised dead cells and lipids. Therefore, drug penetration through the SC is governed via passive diffusion and is described by Fick's law (Equation 1.1).

$$\frac{dM}{dt} = \frac{D \cdot \Delta C \cdot P}{h} \quad 1.1$$

where dM/dt is the steady state flux, D is the drug diffusion coefficient, ΔC is the concentration gradient of the drug across the SC, P is the drug partition coefficient, and h is the thickness of the SC.

The ability of a molecule to passively diffuse through the SC is limited by many factors, including a low molecular weight (MW) (< 500 Da) and a balanced lipophilicity ($\log P$: 1 – 3) (Donnelly, Singh, Morrow, et al., 2012). As a result, various passive approaches rely on optimising and enhancing the drug-vehicle interactions to cause some modifications in the SC structure (Chen et al., 2006; Schuetz et al., 2005).

Examples of passive approaches including prodrugs, eutectic systems, liposomes, vesicles, and chemical enhancers (Zaid Alkilani et al., 2015). However, some of the common limitations associated with passive approaches such as low efficacy, and long lag time in drug release which can be problematic, especially when a rapid onset of action is desired (Karande & Mitragotri, 2009; Marianecci et al., 2014).

On the other hand, active approaches rely on the physical disruption of the SC or using external energy as a driving force for drug penetration enhancement. Examples of active approaches including ultrasound (Azagury et al., 2014; Han & Das, 2015), iontophoresis (Gratieri & Kalia, 2013), electroporation (Pr at & Vanbever, 2002), jet injectors (Stachowiak et al., 2009), radio-frequency heating (J. W. Lee et al., 2011; Lin et al., 2014), and MNs (Damiri et al., 2022; Yu et al., 2021; Zhang et al., 2022). These approaches extend the range of drugs available for dermal delivery and provide more consistent control of the drug release profiles, therefore, reducing lag time associated with drug release as compared to passive approaches (Arora et al., 2008; Mitragotri, 2013).

Among the various active methods, MNs are considered a cost-effective, efficient, and patient-friendly approach for drug delivery to the skin (Yadav et al., 2021; Zaid Alkilani et al., 2015). More details about MNs will be described in the next section.

1.3 Microneedles (MNs)

1.3.1 Definition and history of MNs

MNs are composed of micron-sized arrays of needles attached to a base-plate or patch. Generally, MNs usually have conical or pyramidal shape with a height

ranging from 150 to 1500 μm and a tip diameter between 1 and 25 μm (Gratieri et al., 2013; Indermun et al., 2014; McAllister et al., 2003; Waghule et al., 2019). The MN design and dimensions should allow penetration of the MNs across the SC (thickness: 10 – 20 μm) to the viable epidermis without contact with nerves and blood capillaries located deep in the dermis, avoiding pain or bleeding as compared with the conventional hypodermic injections (Figure 1.2) (Vandervoort & Ludwig, 2008).

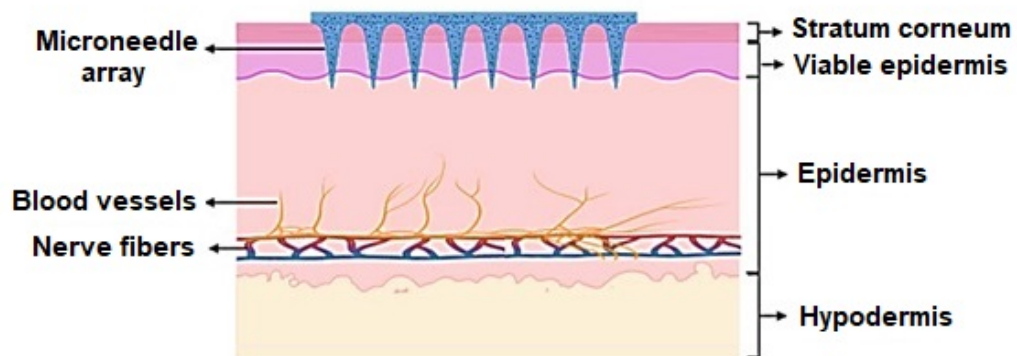


Figure 1.2 MN penetration across the SC. Adapted from Azmana et al. (2020).

The elastic nature of human skin may lead to ineffective MN penetration due to twisting of the skin during MN application, especially for the short or blunt MNs (McAllister et al., 2003). Therefore, the MN geometry (e.g., height, base width, inter-base space, and tip diameter) and shape (e.g., conical, pyramidal, cylindrical, tapered tips) is crucial for proper skin insertion to avoid nerve and blood capillary contact and create efficient pathways for the delivery of drug molecules with multiple size and aqueous solubility (Ashraf et al., 2011; Liu et al., 2014; Van Der Maaden et al., 2012). Furthermore, MNs typically encounter a variety of stresses during insertion or removal and must possess sufficient mechanical strength and elasticity to avoid breaking or bending of the MNs and base-plate fracture (Donnelly et al., 2011; Park et al., 2005;

Zahn et al., 2000). Therefore, mechanical characterisation is an essential step during MN formulation and should be performed to ensure that MNs are safe and efficient prior to use.

MNs allow painless dermal delivery of molecules with various physicochemical properties ranging from small-size molecules like alendronate and ketoprofen to large-size molecules and proteins like vaccines, heparins, and insulin (Gomaa et al., 2012; Katsumi et al., 2012; Kim et al., 2012; Ling & Chen, 2013; So et al., 2009). In addition, the MN approach minimises the dosing variability associated with transdermal drug delivery (McCrudden et al., 2015). Moreover, MN technology reduces the risk of infection at the site of administration due to the fast skin recovery of the created microchannels, decreases the potential of bleeding and cross-contamination, and increases patient compliance due to the ease of self-administration as compared with hypodermal injections (Ameri et al., 2014; Arora et al., 2008; Donnelly, Singh, Garland, et al., 2012; Gill et al., 2008; Indermun et al., 2014; McCrudden et al., 2014; Tuan-Mahmood et al., 2013).

Although transdermal drug delivery via MN system was dreamed up several decades ago, it wasn't until the mid-1970s where the concept gained official acceptance when Martin and Virgil received a US patent for an invention that uses micron-scale needles to deliver therapeutic medicine to patients with a minimum level of pain (Gerstel & Place, 1976; Halder et al., 2021). Research on designing MNs for drug delivery was accelerated in the 1990s by Georgia Institute of Technology, Becton Dickinson, and Alza Corporation (Azmana et al., 2020). MNs were initially fabricated from silicon (Larraneta et al., 2016). However, numerous materials and polymers are currently used to fabricate different types of MNs (Zaid Alkilani et al., 2015). MNs

can be classified based on the fabrication material as metallic, silicon, glass, ceramic, sugar, and polymeric MNs (Chevala et al., 2021).

In the last two decades, the development of MN caught enormous attention from researchers. MN technologies have been subjected to intensive development and research efforts by industrial and academic investigators. As a result, the number of publications in MN formulation and technology has increased steadily in the last few years (Figure 1.3).

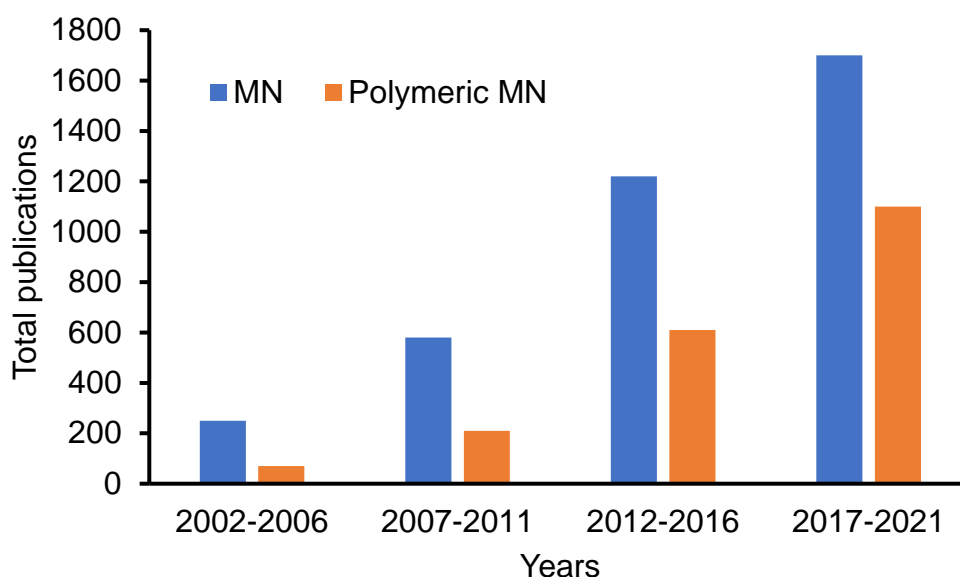


Figure 1.3 Total number of publications on MNs and polymeric MNs over the past 20 years. Adapted from Yadav et al. (2021).

The concept of polymeric MNs was first introduced in 2005 by Yeshurun's research group (Azmana et al., 2020; Yeshurun et al., 2005). Since then, polymeric MNs have drawn the attention of researchers with increased number of publications (Figure 1.3). This can be attributed to the different advantages associated with polymeric MNs over other MN types, including a lower cost of raw material, simpler

fabrication procedures, superior safety, and biocompatibility (Azmana et al., 2020; Chevala et al., 2021).

1.3.2 MN types

Generally, MNs are classified based on the drug delivery mechanism into five groups: solid, coated, hollow, dissolving, and hydrogel-forming MNs (Figure 1.4) (Indermun et al., 2014; Larraneta et al., 2016).

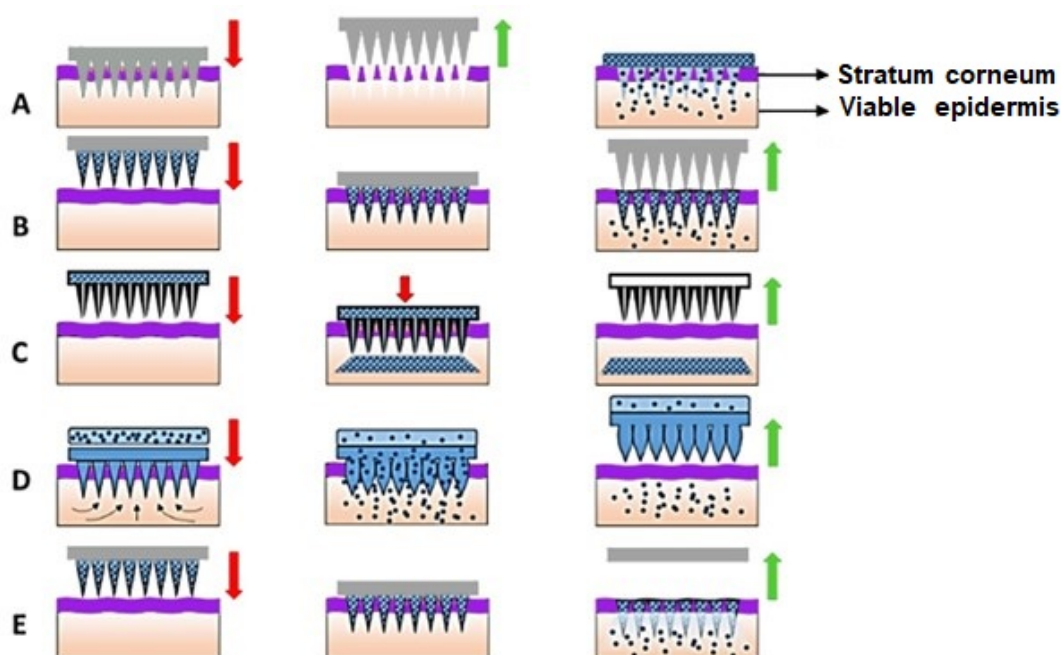


Figure 1.4 Illustrations of the design of (A) solid, (B) coated, (C) hollow, (D) hydrogel-forming, and (E) dissolving MNs. Adapted from Larraneta et al. (2016).

1.3.2(a) Solid MNs

Solid MNs are typically produced from silicon, metals, and polymers (Donnelly, Morrow, McCarron, et al., 2009; Oh et al., 2008). Drug delivery to the skin using solid MNs is a two-step method (Figure 1.4A). Initially, the skin is treated with solid MNs and followed by applying a conventional dosage form such as gel, ointment,

cream, lotion, or patch (Indermun et al., 2014; Schoellhammer et al., 2014). Treating the skin with solid MNs creates microchannels through the SC, allowing passive diffusion of drug molecules from the applied dosage form. However, solid MNs may not enhance drug permeation through some highly viscous formulations (Mitra et al., 2017). In addition, patient convenience may be hampered by the two-step application process of solid MN, which is the main limitation associated with solid MNs (Larraneta et al., 2016; Mitra et al., 2017).

1.3.2(b) Coated MNs

A coated MN is a solid MN coated with a drug formulation before application on the skin (Bariya et al., 2012). Unlike solid MNs, applying coated MNs to the skin is a single-step process (Zaid Alkilani et al., 2015). Upon skin insertion, the coated formulation dissolves, and the loaded drug deposits in the skin (Figure 1.4B). Rapid skin delivery of macromolecules such as vaccines, proteins, peptides, and DNA could be achieved using coated MNs (Tuan-Mahmood et al., 2013). However, coated MNs have limitations, including difficulty achieving uniform dosing due to the uneven coating surface (Chevala et al., 2021). In addition, MNs have a limited surface area and therefore can only be coated with a limited amount of drug. Therefore, coated MNs can only be used for potent molecules or drugs (Zaid Alkilani et al., 2015).

1.3.2(c) Hollow MNs

Hollow MNs can be fabricated with various materials such as metals, silicon, glass, ceramic, and polymers (Chandrasekaran et al., 2003; Ovsianikov et al., 2007; Roxhed, Griss, et al., 2008; Roxhed, Samel, et al., 2008; Sammoura et al., 2007; Wang et al., 2006). In a similar manner to hypodermic needles, hollow MNs are used to

deliver drug solutions into the skin tissues after skin insertion through tiny channels within the MNs (Figure 1.4C). With hollow MNs, liquid drug formulations can be continuously delivered across the skin by diffusion or driven flow (pressure or electrical force) and are thus more effective than solid or coated MNs in delivering larger amounts of drug and allowing the flow rate to be controlled (Van Der Maaden et al., 2012).

The limitations of hollow MNs include the possibility of needle bores clogging by the skin tissues during MN insertion (Gardeniers et al., 2003). In addition, compression of the dermal tissue during MN insertion may resist the flow of the drug solution into the skin (Martanto et al., 2006). However, an MN tip with a sideways bore opening and partial needle retraction after insertion can overcome these two limitations (Griss & Stemme, 2003; Wang et al., 2006). Another limitation of hollow MNs relates to the use of a liquid drug formulation, which requires an appropriate reservoir and is less stable than a solid dosage form (Larraneta et al., 2016).

1.3.2(d) Hydrogel-forming MNs

A hydrogel-forming MN is formulated from swellable polymers attached to a solid base-plate or drug reservoir (Hong et al., 2014). Drugs could be encapsulated within the MN shafts, the base-plate, or an attached drug reservoir (Donnelly, Singh, Garland, et al., 2012). Upon insertion into the skin, the MNs absorb interstitial fluids, resulting in a swollen gel that facilitates the drug release (Figure 1.4 D) (Chevala et al., 2021). Many polymers have been used in hydrogel-forming MNs formulation, including poly(methyl vinyl ether-co-maleic acid), polyvinyl alcohol (PVA), polystyrene-block-poly(acrylic acid) and gelatine methacryloyl (Donnelly, Singh, Garland, et al., 2012; Oh et al., 2022; Peng et al., 2021; Zeng et al., 2021).

A significant advantage of hydrogel-forming MNs is that they are removed intact from the skin, leaving no residual polymer behind. In addition, hydrogel-forming MNs are softened after removal from the skin, thus reducing the risk of infection transmission (Larraneta et al., 2016).

1.3.2(e) Dissolving MNs

The fabrication of dissolving MNs involve drug loading into a matrix of biocompatible sugar or polymer (Dalvi et al., 2021). Upon skin insertion, the needles dissolve when they come into contact with interstitial fluids, releasing the drug payload (Figure 1.4 E). The drug release from dissolving MNs depends on the material's dissolution rate (Larraneta et al., 2016). For example, with some water-soluble sugars such as trehalose and sucrose, the full release might be achieved within 5 min, whereas with some biodegradable polymers such as chitosan and chitin, it might take several days (Kim et al., 2012). Consequently, changing the composition or modifying the MN fabrication process can result in a controlled drug delivery (Larraneta et al., 2016).

Like solid MNs, dissolving MNs can also be used without a drug load as a pretreatment method to increase skin permeability prior to drug application (Kim et al., 2012). Due to the encapsulation of the drug within the MN matrix, dissolving MNs have a notable advantage over coated one with regards to the drug loading in the MN array (Kochhar et al., 2012). In addition, no sharp waste is produced after using dissolving MNs due to the dissolving properties of the MN shafts, eliminating the possibility of accidental cross-contamination (Sartawi et al., 2022).

Dissolving MNs have also been reported to successfully deliver a wide variety of molecules, including small molecules (MW < 500 Da) such as lidocaine,

macromolecules (MW > 500 Da) such as insulin and heparin, hydrophilic molecules such as diclofenac sodium, and lipophilic molecules such as resveratrol (Aung et al., 2021; Caffarel-Salvador et al., 2021; Yang Liu et al., 2021; Silva et al., 2022; Zhu et al., 2022). Moreover, dissolving MNs are applied to the skin in a single-step approach which enhances patient convenience as compared with solid MNs. Based on these advantages, this thesis aims to explore dissolving MNs fabricated with a natural polymer (i.e., RSC) for delivering hydrophilic and hydrophobic drugs to the skin. Therefore, the methods and polymers used for dissolving MNs will be discussed in more detail in the following subsections.

1.3.3 Fabrication of dissolving MNs

The method used for dissolving MN fabrication must be reproducible and able to form MNs with sharp tips to ensure efficient skin penetration. It must also not affect the loaded drug stability. A number of methods have been utilised for dissolving MN fabrication, including solution casting (micro-moulding) (K. Lee et al., 2011), atomised spraying (McGrath et al., 2014), droplet-born air blowing (J. D. Kim et al., 2013), and three-dimensional printing (Figure 1.5) (Pere et al., 2018).

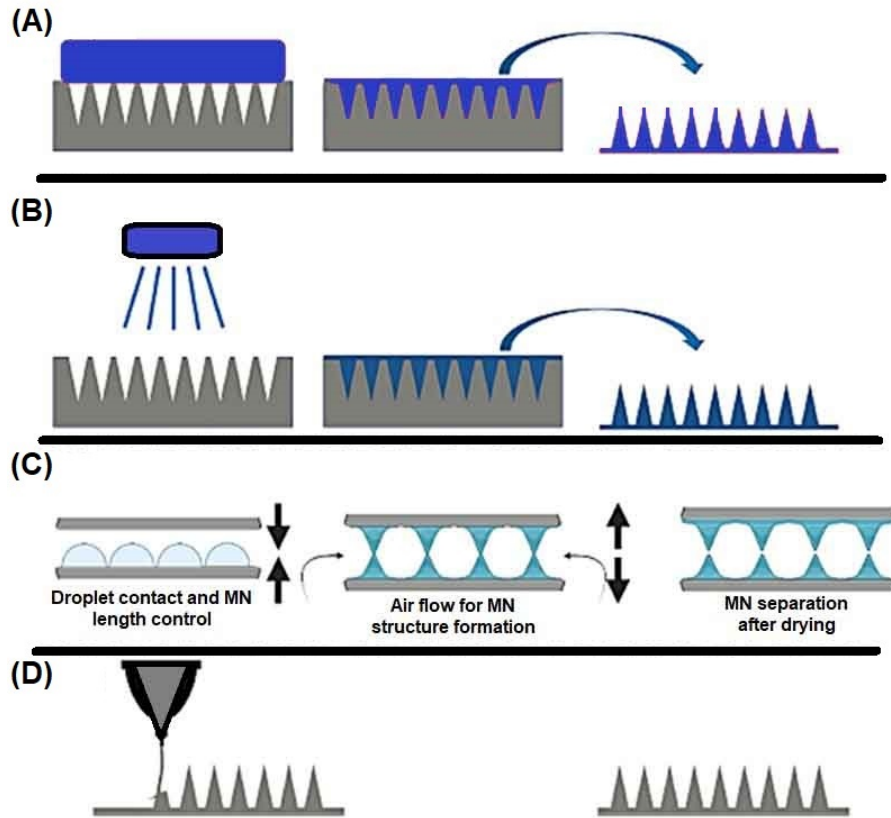


Figure 1.5 Examples of methods commonly used for dissolving MNs fabrication including (A) casting, (B) atomised spraying, (C) droplet-born air blowing, and (D) three-dimensional printing. Adapted from Sartawi et al. (2022).

Solution casting technique is the simplest and most commonly used method for dissolving MN fabrication (Moore et al., 2022; Sartawi et al., 2022). In this technique, a viscous solution, gel, or suspension is cast on a mould with micron-sized cavities. The formulation should be fully distributed over the pores to ensure complete MN array formation. In addition, the fabrication material of the mould should be inert to avoid sticking or interaction with the formulation and to allow easy removal of the dried MN array. After casting, centrifugation or vacuum is applied in order to push the viscous formulation into the mould's cavities. Eventually, the formulation is allowed to dry and solidify before being peeled off (K. Lee et al., 2011).

1.3.3(a) Polymers used in the fabrication of dissolving MNs

During dissolving MN manufacturing process, needle strength is the most important factor because the needle must be inserted into the epidermis without breaking in order to deliver the drug effectively (Yang & Zahn, 2004). Furthermore, the biocompatibility of dissolving MNs with the biosystem is crucial (Wu et al., 2008). As a result, selecting an appropriate polymer for the development of dissolving MNs is essential.

An appropriate material for dissolving MN formulation should possess good mechanical robustness, biocompatibility, and biodegradability. In addition, the material should not affect the potency, safety, and efficacy of the encapsulated drug (Sartawi et al., 2022). Drug release mechanisms from MNs vary according to the design and materials involved. Meanwhile, drug diffusion, dissolution, and degradation of the material matrix are directly responsible for drug release. Moreover, the release kinetics can also be influenced by other factors, including drug-carrier interactions, drug solubility, and drug location within the carrier's matrix (Macha et al., 2019).

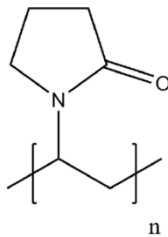
Various materials such as silk, sugars, and polymers have been investigated for dissolving MN development. However, a recent review stated that up to 84 % of drug- and vaccine-loaded dissolving MNs are fabricated from natural, synthetic and semi-synthetic polymers. Polyvinylpyrrolidone (PVP), hyaluronic acid, and poly (methyl vinyl ether-*co*-maleic anhydride) are the most mentioned polymers used for dissolving MN fabrication (Moore et al., 2022). Other polymers used as candidates for dissolving MN fabrication including PVA (Chu et al., 2010), carboxy methyl cellulose (CMC) (Rahman et al., 2021), hydroxypropyl methyl cellulose (HPMC) (Bhadale & Londhe,

2021), poly(methyl methacrylate) (Moon et al., 2005), poly(lactic-co-glycolic acid) (Park et al., 2006), poly(carbonate) (Han et al., 2007), and polysaccharides (Bhadale & Londhe, 2021; Larraneta et al., 2016).

1.3.3(a)(i) Polyvinyl pyrrolidone (PVP)

PVP is an amorphous water-soluble polymer (Chan et al., 2015). Different grades of PVP are commercially available, which are classified based on their viscosity in 1 % w/v solution using K values such as K12, K17, K25, K30, and K90 (Rowe et al., 2009). The MW of PVP ranges between 2500 and 3000000 Da. PVP with a higher K value has a higher MW (Kurakula & Rao, 2020). The physicochemical properties of PVP are shown in Table 1.1.

Table 1.1 Physicochemical properties of PVP. Adapted from Kurakula and Rao (2020).

Property	Description
Chemical structure	 <p>The chemical structure shows a pyrrolidone ring (a five-membered ring with one nitrogen atom and one carbonyl group) attached to a polymer chain. The polymer chain is represented by a carbon atom bonded to two other carbons, with brackets and a subscript 'n' indicating the repeating unit.</p>
Description	Fine, white to off white, hygroscopic, odourless, amorphous powder
MW	2500 – 3000000 Da
Glass transition temperature (T_g)	120 – 174 °C
Solubility	Soluble in water, methanol, ethanol, chloroform, amines, and acids. Insoluble in hydrocarbons, ethers, and mineral oil

PVP is biocompatible, non-toxic, stable, chemically inert, and has good film-forming ability (Haaf et al., 1985). The hydrophilic and hydrophobic functional groups

present within PVP make it an amphoteric compound and soluble in both water and organic solvents (Foltmann & Quadir, 2008; Haaf et al., 1985). The amide group of its monomer unit is highly polar and the methylene groups of its main chain and ring are non-polar (Table 1.1). Therefore, it has been widely employed as a carrier in the pharmaceutical, biomedical, and nutraceutical fields (Husain et al., 2018).

Several PVP-based systems have been developed to deliver different synthetic and natural active compounds. PVP has been used in a variety of pharmaceutical formulations such as solid dispersions (Chan et al., 2015), tablets (Patel et al., 2004), hydrogels (Yu et al., 2007), nanofibers (Yubo Liu et al., 2021), buccal films (Jovanović et al., 2021), and MNs (Park et al., 2019; Xu et al., 2022; Yang et al., 2021).

PVP has been widely utilised solely or blended with other polymers for dissolving MN formulation (Amodwala et al., 2017; Chen et al., 2020; Chu et al., 2010; Ronnander et al., 2020). Aung et al. (2020) formulated dissolving MNs from a polymer blend of PVP and HPMC (50 %w/w) loaded with alpha-arbutin (8 %w/w). PVP-HPMC MNs increased the alpha-arbutin permeation by ~ 2 folds as compared with MNs formulated with Gantrez™ S-97. Chen et al. (2020) reported that the Parafilm® penetration was the highest in PVP MNs as compared with dissolving MNs composed of PVA, hyaluronic acid, HPMC, or CMC. Therefore, PVP is suitable for the fabrication of dissolving MNs with desired mechanical strength and skin insertion.

1.3.3(a)(ii) Polyvinyl alcohol (PVA)

PVA is a semicrystalline water-soluble synthetic polymer and is among the world's most widely produced synthetic polymers (Teodorescu et al., 2019). The chemical formula of PVA is $(C_2H_4O)_n$, where n represents the polymeric chain length

(Brough et al., 2016). Commercially available PVA products have an n value between 500 and 5000, equivalent to an MW between 20000 and 200000 Da (Rowe et al., 2009). A unique feature of PVA is that the monomer, vinyl alcohol, cannot exist in the free state. Therefore, PVA is produced by the hydrolysis of polyvinyl acetate (Brough et al., 2016).

PVA is odourless, nontoxic, biodegradable with excellent high tensile strength and flexibility (Ibrahim et al., 2010). These advantages, in addition to acceptable cost, result in utilising PVA for various applications such as packaging and pharmaceutical industries (Ibrahim et al., 2010). The physicochemical properties of PVA are listed in Table 1.2.

Table 1.2 Physicochemical properties of PVA. Adapted from Brough et al. (2016)

Property	Description
Chemical structure	$\left[\text{CH}_2 - \underset{\text{OH}}{\text{CH}} \right]_n$
Description	White to off white- semi-crystalline powder
Available MW	14,000 – 205,000 g/mol for partially hydrolyzed grades; 16,000 – 195,000 g/mol for fully hydrolysed grades
Melting point (T_m)	180 – 240 °C
T_g	40 – 80 °C
Solubility	Very soluble in water. Insoluble in most organic solvents. Slightly soluble in ethanol, practically insoluble in acetone

PVA has been used in a variety of pharmaceutical applications. It is used in emulsions (Galindo-Rodriguez et al., 2004), topical gels (Abdel-Mottaleb et al., 2009), ophthalmic solutions (Bourges et al., 2006), transdermal patches (Davaran et al., 2005), and MNs (Zhang et al., 2021).

Owing to its favourable properties, PVA has been employed in the fabrication of different MN types, including coated (Gill & Prausnitz, 2008), swellable (Yadav et al., 2022), and dissolving MNs (Chu et al., 2010; Gill & Prausnitz, 2008). McGrath et al. (2014) reported that dissolving MNs fabricated with PVA have superior skin penetration as compared with MNs having similar geometry composed of raffinose, trehalose, PVP, CMC, HPMC, and sodium alginate.

1.3.3(a)(iii) Polysaccharides

Dissolving and biodegradable MNs can be easily formulated using polysaccharide solutions (Lee et al., 2008). Drug molecules are incorporated into the solution before the casting step. Some polysaccharides are tough, biodegradable, biocompatible, cheap, and safe, thus drawing increasing attention for dissolving MN fabrication (Miyano et al., 2005). Examples of polysaccharides used in MN fabrication are hyaluronic acid (Kim et al., 2018; Larrañeta et al., 2018; Liu et al., 2012), cellulose derivatives (Bayarri et al., 2009; Dhar et al., 2012; Lee et al., 2008), chitosan (Chen et al., 2012; Dhar et al., 2012), amylopectin (Lee et al., 2008), and starch (Ling & Chen, 2013).

Starch is a polysaccharide that has been widely investigated for packaging and biomedical purposes owing to its good film-forming ability and ease of processing (Alrimawi et al., 2021; Rodrigues & Emeje, 2012). However, only a few reports

investigated starch as a biopolymer for MN fabrication. Ling and Chen (2013) formulated dissolving MNs using a combination of wheat starch and gelatine (50 %w/w) for transdermal delivery of insulin. The starch-gelatine MNs could penetrate rat skin and completely dissolve within 5 min. In addition, the stability of insulin within the MN matrix at ambient temperatures was greater than 90 % for 30 days, indicating the cost-effectiveness and convenience of starch-gelatine MNs for insulin delivery.

Pineda-Álvarez et al. (2020) investigated a blend of wheat starch and gelatine (15:145) for developing dissolving MNs to deliver losartan potassium (15 %w/w) through the skin. The drug was loaded as a free powder or nanoparticles. The fracture force was ~ 3.2 N for the nanoparticles-loaded MNs, while it was ~ 4 N for the powder-loaded MNs. The results showed that the starch-gelatine MNs loaded with losartan nanoparticles have ~ 4-folds higher flux as compared with MNs loaded with losartan powder.

Chemical derivatives of starch such as hydroxyethyl starch and amylopectin have been investigated for MN fabrication (Y.-H. Park et al., 2016; Park & Kim, 2017; Y. Park et al., 2016; Poirier et al., 2017). Nevertheless, to date, studies by Ling and Chen (2013) and Pineda-Álvarez et al. (2020) are the only literature investigating starch as a polymer for MN fabrication. However, in both studies, starch was blended with a high amount of gelatine (50 – 90 %w/w) to overcome the poor mechanical properties of starch. In addition, the physicochemical, mechanical, and skin insertion properties were not thoroughly investigated. Therefore, the current work will focus on starch as a major component for dissolving MNs fabrication with a thorough

investigation of the physicochemical, mechanical, and skin insertion properties of the starch-based MNs. More details about starch are mentioned in the following part.

1.4 Starch

Starch is a biodegradable, cheap, abundant, and non-toxic polysaccharide with good film-forming ability. Therefore, starch is one of the most explored and promising biodegradable materials for producing biodegradable products in packaging, food, and pharmaceutical industries (Jha et al., 2020; H.-S. Kim et al., 2013; Saberi et al., 2015; Suh et al., 2020).

Starch consists mainly of two types of molecules, amylose and amylopectin (Figure 1.6). The major component of starch is amylopectin, which is a large, highly branched polymer consisting of α -1,4 linked *d*-glucose units with branches linked by α -1,6 bonds (Kaufman et al., 2015). Amylose is a linear polymer of α -1,4 linked *d*-glucose units. Amylose is the key component involved in water absorption, swelling, and gelation of starch (Hoseney, 1994). Compared to amylopectin, pure amylose has a very stable structure and a solid molecular orientation, resulting in denser and stronger films than amylopectin (Lourdin et al., 1995). In addition, linear chains of amylose are more likely to interact by hydrogen bonds, enabling them to produce self-supporting films as compared with the branched amylopectin chains (Wittaya, 2012). Amylose content is usually 20 – 30 %w/w of total starch content (Kaufman et al., 2015).

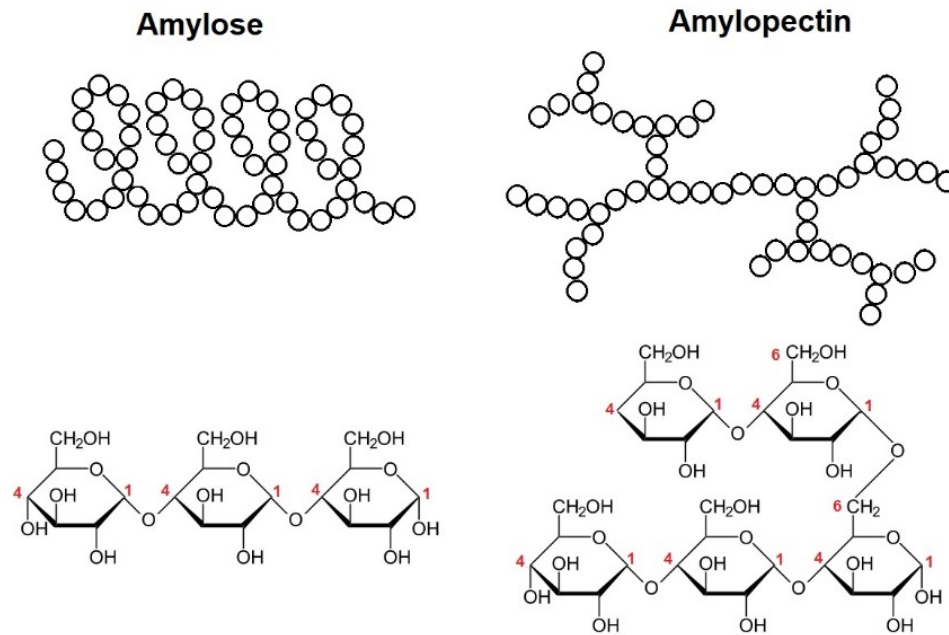


Figure 1.6 Structure of amylose and amylopectin. Adapted from Willfahrt et al. (2019).

Starch can be extracted from many sources, including wheat, rice, potato, maize, cassava, sorghum, barley, sweet potato, mung bean, and sago (Vamadevan & Bertoft, 2015). The composition and properties of starch granules vary considerably depending on year-to-year variations, place of growth, plant variety, methods of starch isolation, and analytical methods used (Asaoka et al., 1985; Gérard et al., 2001).

1.4.1 Gelatinisation and retrogradation

When starch granules are heated in the presence of water, a process known as starch gelatinisation occurs (Ratnayake & Jackson, 2008). The gelatinisation process involves an irreversible disorder transition of amylose and amylopectin chains of starch granules (Maaruf et al., 2001; Sanchez-Gonzalez et al., 2015). During the gelatinisation process, a number of phenomena are observed, including granule swelling, amylose solubilisation, heat uptake, increased viscosity, and crystallinity loss

(Maaruf et al., 2001; Tan et al., 2004). Generally, the properties of starch-based formulations are regulated by gelatinisation (Sanchez-Gonzalez et al., 2015). Gelatinisation is required to get the film-forming properties and allows interactions with other polymers to enhance the mechanical properties of starch (Sanchez-Gonzalez et al., 2015).

Gelatinisation is a two-step process. The first step involves the swelling of starch granules as a result of hydrogen bond breaking in the amorphous portions of the starch (Figure 1.7B). The second step involves the amorphous regions to be hydrated and swelled with water acting as a plasticiser (S. Wang et al., 2015). Slade and Levine (1988) mentioned that the amorphous regions of starch must first melt or go through a glass transition for gelatinisation to take place. As a result, the polymeric molecules, particularly those of amylose, leach out of the starch granules, leading to increased matrix viscosity (Biliaderis, 1991; Eerlingen & Delcour, 1995).

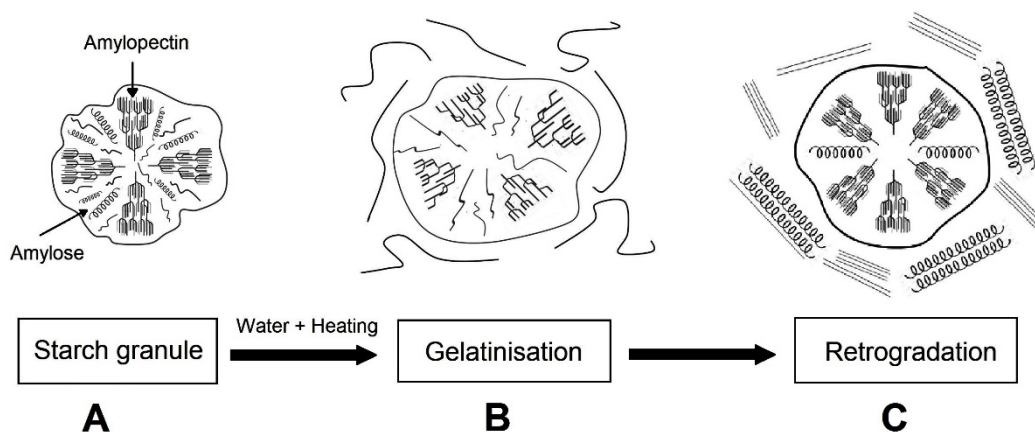


Figure 1.7 Illustration of starch gelatinisation and retrogradation. Adapted from del Carmen Robles-Ramírez et al. (2012).

As the gelatinised starch cools down, the starch chains (amylose and amylopectin) reassociate, forming a more ordered structure in a process called